Morphology, Microstructure, and Magnetic Properties of Ordered Large-Pore Mesoporous Cadmium Ferrite Thin Film Spin Glasses

Christian Reitz,[†] Christian Suchomski,[†] Venkata Sai Kiran Chakravadhanula,[†,⊥] Igor Djerdj,[‡] Zvonko Jagličić,[§] and Torsten Brezesinski*[,†]

[†]Institute of Nanotechnology, Karlsruhe Institute of Technology, Hermann-von-Helmholtz-Platz 1, 76344 Eggenstein-Leopoldshafen, Germany

[‡]Ruđer Bošković Institute, Bijenička 54, 10000 Zagreb, Croatia

[§]Institute of Mathematics, Physics and Mechanics & Faculty of Civil and Geodetic Engineering, University of Ljubljana, Jadranska 19, 1000 Ljubljana, Slovenia

ⓢ Supporting Information

ABSTRACT: Herein, we report the synthesis, microstructure, and magnetic properties of cadmium ferrite ($CdFe_2O_4$) thin films with both an ordered cubic network of 18 nm diameter pores and single-phase spinel grains averaging 13 nm in diameter. These mesoporous materials were produced through facile polymer templating of hydrated nitrate salt precursors. Both the morphology and the microstructure, including cation site occupancy and electronic bonding configuration, were analyzed in detail by electron microscopy, grazing incidence small-angle X-ray scattering, Raman and X-ray photoelectron spectroscopy, and N_2-physisorption. The obtained data demonstrate that the network of pores is retained up to annealing temperatures as high as 650 °C—the onset of crystallization is at $\vartheta = (590 \pm 10)$ °C. Furthermore, they show that the polymer-templated samples exhibit a "partially" inverted spinel structure with inversion parameter $\lambda = 0.40 \pm 0.02$. This differs from microcrystalline $CdFe_2O_4$ which shows virtually no inversion. Magnetic susceptibility studies reveal ferrimagnetic spin coupling below 147 K and further point to the likelihood of glassy behavior at low temperature ($T_f \approx 60$ K). In addition, analysis of room temperature magnetization data indicates the presence of sub-10 nm diameter superparamagnetic clusters in an otherwise paramagnetic environment.
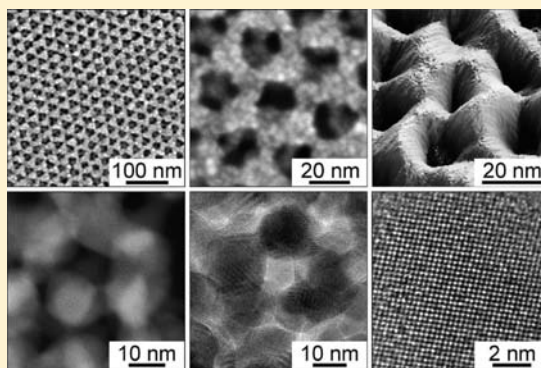
INTRODUCTION

Ordered mesoporous metal oxides in the form of thin films and nanopowders have received significant attention over the past several years. This is due in part to the fact that such interface-controlled materials often exhibit novel properties because of the large surface-to-volume ratio and smaller dimensions. Furthermore, many such materials have been shown to be able to outperform their bulk counterparts which is particularly evident in the fields of electrochemical energy storage, catalysis, and information technology.[1−5]

Advances in both polymer templating and processing of sol−gel derived coatings have enabled the preparation of a range of different metal oxides with ordered pore cavities ranging from a few nanometers to almost 40 nm in diameter.[5−10] Their formation relies on the coassembly of molecular precursors with an amphiphilic polymer using an evaporation-induced self-assembly (EISA) process.[11−13] Despite the progress made, many of the mesoporous materials described in the literature exhibit either only partially crystalline walls or an ill-defined porosity after thermal annealing. Part of the reason for that is the difficulty of controlling the amorphous-to-crystalline conversion—amorphous wall structures often cannot be crystallized with retention of both the porosity and the periodicity because of mismatches between the stable crystallite size and pore wall thickness.

Assembly of preformed nanocrystal building blocks into 3-dimensional architectures has been shown to be a viable alternative to overcome this issue.[2,14,15] However, the synthesis of suitable nanocrystals that are "soluble" in EISA-compatible solvents is time-consuming and not straightforward. Nevertheless, both Tolbert et al. and Milliron et al. have recently demonstrated that the use of ligand-stripped nanocrystal building blocks is promising for the synthesis of mesoporous materials.[16,17] While the architectures reported in their works were mostly disordered, they showed that this methodology can be applied to different nanocrystals.

In the present work, we report the morphology, microstructure, and magnetic properties of sol−gel derived, ordered large-pore mesoporous cadmium ferrite ($CdFe_2O_4$) thin films.

These materials were fabricated through facile polymer templating of hydrated nitrate salt precursors. By taking advantage of the superior templating properties of a poly-(ethylene-co-butylene)-block-poly(ethylene oxide) diblock copolymer, it was possible to convert the initially amorphous pore walls to highly crystalline, single-phase spinel while preserving the nanoscale structure. We note that this type of polymer has been shown to produce materials with comparatively thick walls that typically allow for uniform nucleation and growth of the crystalline phase in such way that the pore-solid architecture is only affected to a limited extent.[3,8,18]

Cadmium ferrite belongs to the spinel-type oxides with space group $Fd\bar{3}m$ (O_h^7). Compared to other transition metal ferrites such as $CoFe_2O_4$ and $ZnFe_2O_4$, it has not received much attention in the literature for unknown reasons. Nonetheless, $CdFe_2O_4$ has been shown to have potential for use in magneto-optical devices and as semiconducting sensing material.[19−21] In general, spinel ferrites exhibit a variety of interesting electrical, optical, and magnetic properties which is why they are widely used in applications such as magnetic recording.[22−24] While single-magnetic cation ferrites, including $CdFe_2O_4$ and $ZnFe_2O_4$, seem to be of less interest for such applications, it is known that the physical properties can be effectively tailored through the cation distribution among the octahedral and tetrahedral sites.[25,26] In recent years, it has been shown that the cation site occupancy can be strongly affected by (1) the grain size (finite size effects), (2) material morphology, and (3) the processing conditions.[27−31] As a result, nanocrystalline ferrites whether prepared by chemical solution deposition or physical deposition techniques exhibit properties that are distinct from their microcrystalline (bulk) counterparts. The strong dependence of the material properties on the cation distribution is for example reflected in the variety of magnetic ordering phenomena (ranging from ferrimagnetism to spin glass behavior) that have been observed in the past two decades.[32−34] This variety and the fact that the spinel-motif structure enables materials with tailor-made properties to be produced has renewed the interest in spinel ferrites, in particular nanocrystalline forms of these materials.

As mentioned above, here we report for the first time the templating synthesis of ordered large-pore mesoporous $CdFe_2O_4$, a ternary oxide that, as is shown, can be produced with a nanocrystalline framework. We use these thin films as model system to study the magnetic properties and the microstructure relative to bulk material. Overall, the polymer-templated thin films exhibit interesting magnetic behavior over a wide temperature range and might lend themselves to nanomagnetic host/guest applications (e.g., magnetically exchange-coupled composites).

■ EXPERIMENTAL SECTION

Materials. A 42 mg portion of $H[(CH_2CH_2)_{0.67}$-$(CH_2CHCH_2CH_3)_{0.33}]_{89}(OCH_2CH_2)_{79}OH$, referred to as KLE,[35,36] 252 mg of $Fe(NO_3)_3 \cdot 9H_2O$ (99.99%), and 96 mg of $Cd(NO_3)_3 \cdot 4H_2O$ (99.99%) are dissolved in a mixed solvent of ethanol (1.4 mL) and 2-methoxyethanol (0.6 mL). Once the solution is clear, thin films can be produced via dip-coating on polar substrates, including partially oxidized Si(100) wafers and quartz glass. Optimal conditions include relative humidities of (12 ± 2) %. For best results, the as-made samples are transferred to an oven at 80 °C for 12 h and then heated to 300 °C using a 44 min ramp followed by aging for 6 h; nonporous powder material was prepared under identical conditions. To remove the polymer template and to fully crystallize the amorphous inorganic

walls, the thin films are heated to 650 °C at a rate of 5 °C·min⁻¹ followed by subsequent quenching to room temperature.

Methods. Both top view and cross-sectional scanning electron microscopy (SEM) images were taken with a MERLIN from Carl Zeiss. The Titan 80-300 (FEI) transmission electron microscope was used to study the morphology, structure, and chemical composition of the polymer-templated thin films by high-resolution TEM (HRTEM), selected-area electron diffraction (SAED), Z-contrast imaging, and elemental mapping. Drift-corrected elemental mapping using an EDX detector was performed in the scanning transmission electron microscopy mode with a high-angle annular dark field detector (STEM-HAADF). Tapping mode AFM images were collected on a multimode AFM from Veeco Instruments employing Olympus microcantilevers (resonance frequency: 300 kHz; force constant: 42 N·m⁻¹). X-ray diffraction (XRD) measurements were carried out on both a Bruker D8 Discover diffractometer in grazing incidence geometry and an X'Pert PRO diffractometer from PANalytical instruments in Bragg−Brentano geometry. Grazing incidence small-angle X-ray scattering (GISAXS) patterns were collected at the German synchrotron radiation facility HASYLAB at DESY on beamline BW4 using a MarCCD area detector. The sample-to-detector distance was approximately 1820 mm. X-ray photoelectron spectroscopy (XPS) data were acquired on a VersaProbe PHI 5000 Scanning ESCA Microprobe from Physical Electronics with mono-chromatic Al−Kα X-ray source and a hemispherical electron energy analyzer at a 45° electron takeoff angle. The C 1s signal from adventitious hydrocarbon at 284.8 eV was used as energy reference to correct for charging. Raman spectra were collected on the SENTERRA dispersive Raman microscope from Bruker Optics equipped with an objective from Olympus (MPlan N 50x; FN = 22; NA = 0.40) and a Nd:YAG laser (λ = 532 nm; P = 2 mW). Nitrogen physisorption experiments were conducted at 77 K using the Autosorb-6 automated gas adsorption station from Quantachrome Corporation. Optical absorption measurements were carried out on a Perkin-Elmer Lambda 900 UV−vis−NIR spectrophotometer. A substrate made from fused silica and an aluminum mirror served as reference for transmission and reflection measurements, respectively. Thermogravimetric analysis (TGA) data were obtained with a Netzsch STA 409 PC. The thermobalance was coupled to a Balzers QMG 421 quadrupole mass spectrometer. The ionization energy was 70 eV. The film thickness was determined with an Alpha Step IQ Surface Profiler from KLA Tencor. For crystal structure visualization, the software Crystal Impact Diamond version 3.2i was used. Magnetic susceptibility measurements were carried out on a Quantum Design superconducting quantum interference device (SQUID) magnetometer (MPMS-XL-5).

■ RESULTS AND DISCUSSION

The mesoporous $CdFe_2O_4$ spinel thin films studied here were fabricated by solution-phase coassembly of sol−gel precursors with a poly(ethylene-co-butylene)-block-poly(ethylene oxide) diblock copolymer, referred to as KLE.[3,8,18] During this research, we found that the use of hydrated cadmium and ferric nitrate salts gives the best results in terms of pore structure and material homogeneity. Synthesis carried out using other precursor combinations such as chlorides and acetylacet-onates failed or produced ill-defined materials (not shown) likely because of both the different sol−gel behavior and the different interactions with the KLE diblock copolymer. This result is in line with our previous work on α-Fe_2O_3.[3] Therein, we showed that high-quality mesoporous thin films can be synthesized through facile polymer templating of hydrated ferric nitrate.

In short, in a typical synthesis, both inorganic salt precursors and the KLE diblock copolymer are dissolved in a mixed solvent of ethanol and 2-methoxyethanol. After stirring the resulting auburn solution for a few minutes, thin films can be produced via dip-coating on virtually any polar substrate.

Thermal treatment can then be used to drive condensation, make the material porous, and to induce crystallization of the initially amorphous pore walls. 2-Methoxyethanol was used as cosolvent in the synthesis because previous work on other transition metal ferrites, including $CuFe_2O_4$, $CoFe_2O_4$, and $NiFe_2O_4$, has shown that it helps obtain mesoporous materials with a more ordered structure.[37−39] We believe that this is due in part to the fact that the forming inorganic/organic composite films remain in a quasi-fluid state for a longer time period during the self-assembly process because of the lower vapor pressure of 2-methoxyethanol compared to other EISA-compatible solvents. However, the use of a two-component mixed solvent with only 30 vol. % 2-methoxyethanol is beneficial to reduce the drying time.

As mentioned above, in the present work we incorporated the amphiphilic diblock copolymer KLE as structure-directing agent. This polymer has been shown to possess many desirable templating properties even though only cubic superstructures can be achieved. More important, however, is the fact that KLE-derived materials accommodate walls sufficiently thick to allow for uniform crystallization while retaining both the nanoscale porosity and the periodicity. These features make it very attractive for the preparation of complex oxide materials with nanocrystalline walls and pore cavities ranging from 15 to 25 nm in diameter.

The pore structure of the KLE-templated $CdFe_2O_4$ spinel thin films at the top surface and in the bulk was analyzed as a function of annealing temperature by a combination of scanning electron microscopy (SEM), transmission electron microscopy (TEM), atomic force microscopy (AFM), and grazing incidence small-angle X-ray scattering (GISAXS). Panels (a−d) of Figure 1 show both the top view SEM and bright-field TEM images at different magnifications of an approximately 400 nm thick film heated to 600 °C. SEM imaging reveals a well-defined network of open 18 nm diameter pores at the hexagonal top surface—the presence of a sealing layer can be ruled out—and further indicates that the pore cavities exhibit a high degree of ordering in the direction parallel to the plane of the substrate. The pore size of 18 nm is confirmed by TEM. From SEM it can also be seen that the films are crack-free on the micrometer length scale (see also low-magnification SEM images in Supporting Information, Figure S1) and that the walls have a thickness of more than 10 nm. The latter observation provides an explanation for the fact that the mesoporous morphology is preserved after crystallization. However, we note that the material seems to be only semicrystalline after heating to 600 °C.

Panels (e−g) of Figure 1 display the structural data from microscopy studies on the same KLE-templated $CdFe_2O_4$ thin film but after thermal treatment at 650 °C. These data are generally consistent with the TEM and SEM observations in that they show a 3-dimensional network of interconnected pores—the pores persist throughout the bulk of the films. In addition, tapping mode AFM verifies that the top surface is fairly flat with a root-mean-square (rms) roughness of only a few nanometers. Nevertheless, it can be clearly seen that the morphology is different and that the pore ordering is weaker (see also SEM image obtained after heating the film to 700 °C in Supporting Information, Figure S1 for comparison). This structural transformation toward more disorder is likely due to progressive crystallization and partial grain growth.

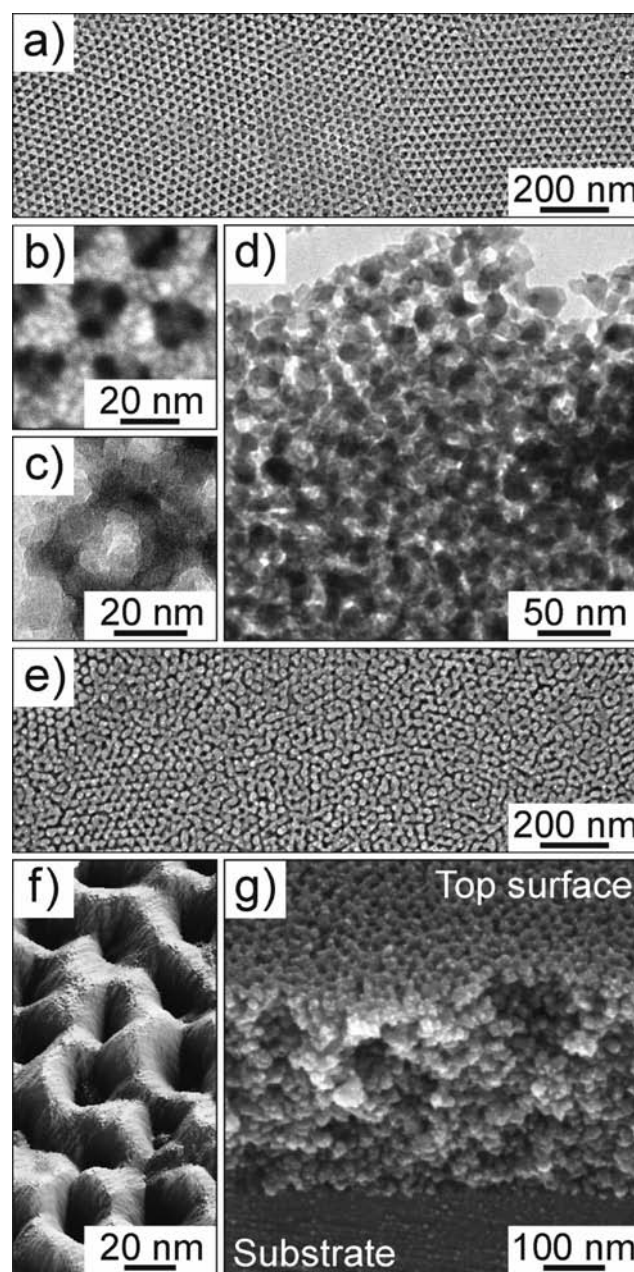In addition to SEM and AFM, high-resolution TEM (HRTEM) and scanning TEM (STEM) images, selected-area

Figure 1. Morphology of KLE-templated $CdFe_2O_4$ spinel thin films heated to 600 °C (a−d) and 650 °C (e−g). (a, b, e) Top view SEM images. (c, d) Bright-field TEM images. (f) 3D tapping mode AFM height image at a tilt of 51°. (g) Cross-sectional SEM image at a 45° tilt showing that the pore structure persists throughout the bulk of the films.

electron diffraction (SAED) patterns, and STEM-EDX elemental maps were collected on the sol−gel derived material heated to 650 °C in air. These data (see Figure 2) provide further insight into the microstructure. The low-magnification STEM image in panel (a) shows the typical morphology of the KLE-templated thin films. From SAED and HRTEM in panels (b, c) we are able to establish that the pore walls are highly crystalline and consist of randomly oriented, spherical grains with a size of approximately (12 ± 2) nm: no amorphous regions were observed (see also STEM and HRTEM images at different magnifications in Supporting Information, Figure S2). This dimension is in line with the results from XRD in Figure
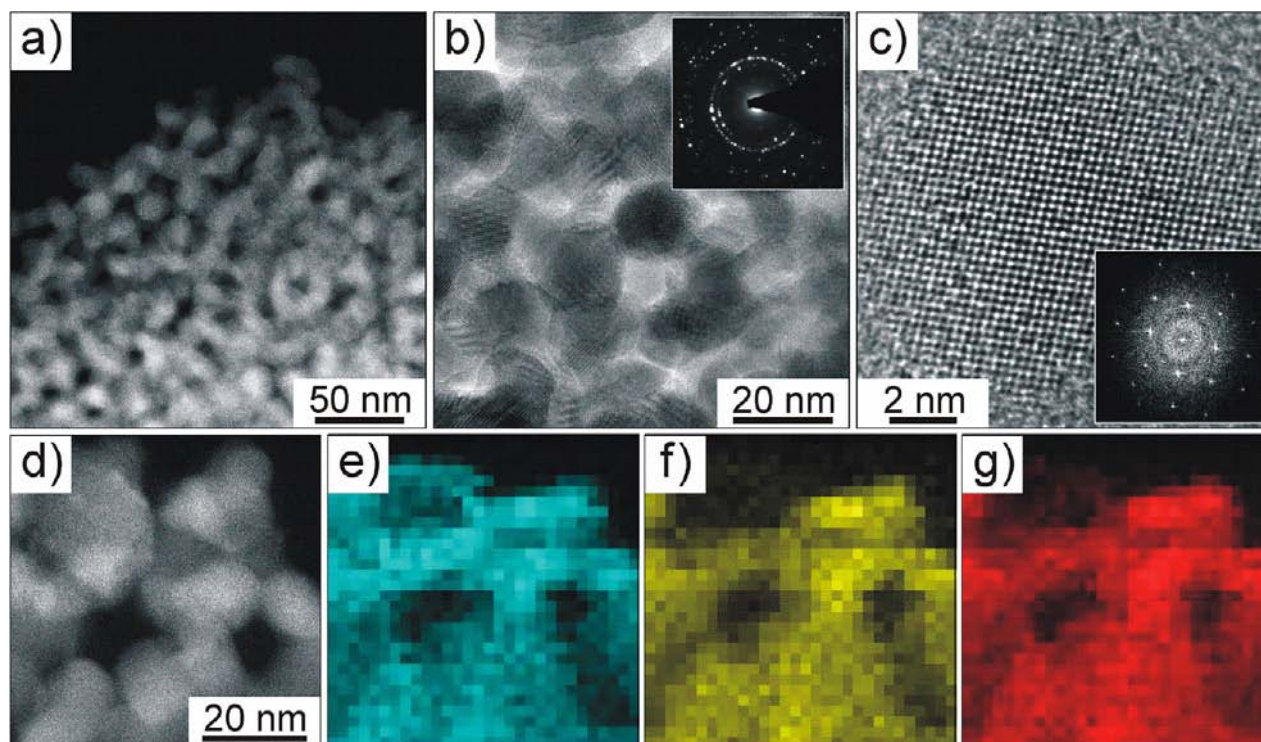
Figure 2. Microstructure of KLE-templated $CdFe_2O_4$ spinel thin films heated to 650 °C. (a) STEM-HAADF image. (b, c) HRTEM images at different magnifications. The inset in panel (b) is an SAED pattern showing Debye−Scherrer rings characteristic of $CdFe_2O_4$ spinel with space group $Fd\bar{3}m$ (O_h^7). A fast Fourier transformation in the zone axis $[0{-}11]$ is depicted in panel (c). (e−g) STEM-EDX elemental maps of the region shown in panel (d); Cd(L) in (e), Fe(L) in (f), and O(K) in (g). The pixel resolution is 2 nm by 2 nm.

6a. The d-values of the reflections in the SAED pattern are in good agreement with those obtained from the JCPDS (Joint Committee on Powder Diffraction Standards) reference card no. 22-1063 for cubic $CdFe_2O_4$, thereby indicating that the films in fact adopt the spinel structure with space group $Fd\bar{3}m$ (O_h^7) at room temperature. The fast Fourier transformation of the HRTEM image in panel (c) reveals the single crystalline nature (zone axis $[0{-}11]$) of the individual nanograins. The STEM-EDX elemental maps in panels (e−g) confirm the nearly uniform distribution of Cd, Fe, and O. Overall, the microscopy data in Figures 1, 2, and Supporting Information, Figure S1 and S2 verify that $CdFe_2O_4$ can be templated to produce mesoporous thin films with both a nanocrystalline spinel structure and good thermal stability.

As mentioned above, the evolution of the pore structure during thermally induced cross-linking and conversion of the initially amorphous material to single-phase spinel was also studied by GISAXS. Figure 3 shows GISAXS patterns at an angle of incidence $\beta = 0.2°$ obtained on a KLE-templated thin film heated to different annealing temperatures. Panels (a, b) indicate that samples with both amorphous and semicrystalline walls produce patterns with distinct maxima. These maxima are typical of a cubic pore structure. The fact that the relative intensity of the scattering maximum in the z-direction (off-plane) is weaker than that of the other reflections is related to the intensity scaling and the morphological anisotropy of the films with significantly fewer repeat units normal to the plane of the substrate. This hypothesis is supported by SAXS in Bragg−Brentano geometry using a strip detector (see Supporting Information, Figure S3). Such measurements only provide information about the periodicity in the off-plane direction. The fact that samples with an amorphous framework show
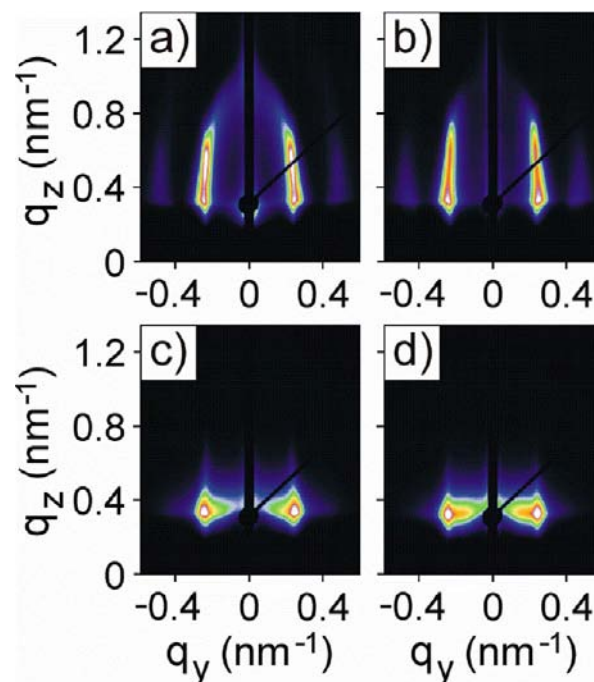

Figure 3. GISAXS patterns at an angle of incidence $\beta = 0.2°$ obtained on a KLE-templated $CdFe_2O_4$ thin film after thermal annealing at 300 °C (a), 600 °C (b), 650 °C (c), and 700 °C (d).

strong first order and weak second order reflections confirms the pore ordering/periodicity in the direction normal to the plane of the substrate. The elliptical shape of the GISAXS patterns further indicates that the KLE-templated thin films undergo unidirectional lattice contraction (approximately 75%

after 6 h aging at 300 °C). The in-plane scattering maxima are virtually unaffected. Such large contraction is not surprising in view of the fact that hydrated nitrate salt precursors were used in the synthesis: both the nitrate ligands and in situ generated hydroxyl groups decompose to H_2O and NO_x during thermal annealing, resulting in a comparatively large mass loss, as evidenced by thermogravimetric analysis (TGA) (see Figure 4).
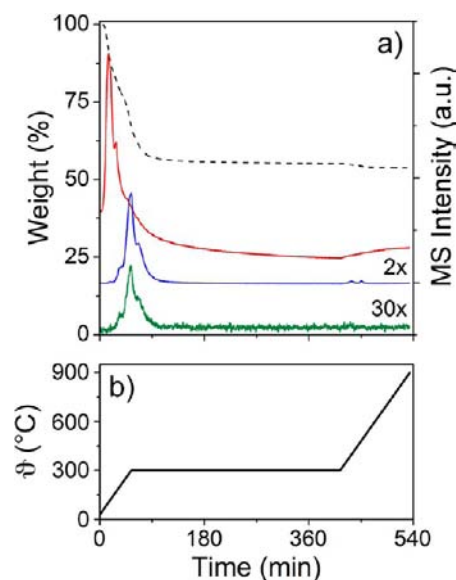

Figure 4. (a) TGA-MS data for a mixture of hydrated cadmium and ferric nitrate salts measured in the temperature range between 30 and 900 °C in synthetic air. The heating rate was 5 °C·min^{-1} with a 6 h aging step at 300 °C. The dashed line represents the TGA curve. The MS analysis shows H_2O ($m/e = 18$) in red, NO ($m/e = 30$) in blue, and NO_2 ($m/e = 46$) in green. (b) Scheme of the heating profile.

Nevertheless, the films do not show any cracks (see SEM images in both Figure 1 and Supporting Information, Figure S1), which suggests that they can readily accommodate the volume changes by flexing of the pore cavities. Higher annealing temperatures do not lead to further off-plane contraction because the sol–gel derived material is highly cross-linked and mostly dehydrated, in a glassy state, after aging at 300 °C. From the GISAXS patterns in panels (c, d) it is apparent that temperatures above 600 °C lead to complete loss of off-plane scattering. The reason for this loss is most likely also related to the morphological anisotropy of the films and changes in pore structure during crystallization and grain growth. In addition, the appearance of diffuse in-plane maxima at lower q-values is observed. These maxima arise because of restructuring (see also microscopy images in both Figure 1 and Supporting Information, Figure S1) and, thus, they become more intense as the annealing temperature is increased from 650 to 700 °C. However, the results with GISAXS are consistent with those from electron microscopy and provide evidence that the wall structure is sufficiently thick to allow for uniform nucleation and growth of the spinel phase while mostly preserving the initial nanoscale structure.

Thermogravimetric analysis-mass spectrometry (TGA-MS) was used as a means of both better understanding the thermally induced lattice contraction and obtaining insight into the formation of glassy $CdFe_2O_4$. Figure 4 shows TGA-MS data of powder material prepared without any KLE diblock copolymer and 2-methoxyethanol but under otherwise identical con-

ditions. It can be clearly seen that the conversion of the hydrated nitrate salts to glassy $CdFe_2O_4$ is essentially completed after 6 h aging at 300 °C. This result is in agreement with previous studies on the thermal decomposition of various hydrated metal nitrates.[40−42] Both $Fe(NO_3)_3 \cdot 9H_2O$ and $Cd(NO_3)_2 \cdot 4H_2O$ are known to dissolve in their own water of crystallization at temperatures below 100 °C. This process is accompanied by (1) dehydration and (2) formation of hydroxy nitrate species because of partial hydrolysis. From TGA-MS it is also evident that the nitrate and hydroxyl groups decompose in several steps to NO/NO_2 and H_2O, respectively, between 150 and 300 °C. As a result, different ferric and cadmium hydroxy- and oxynitrate species, including $M(OH)_x(NO_3)_y$ and $MO_x(NO_3)_y$, are formed which then convert to glassy $CdFe_2O_4$. We note that the discrepancy between measured and theoretical mass loss (46% versus 74%) can be attributed to the procedure of making the powder starting material (see Experimental Section), which already induced partial dehydration and hydrolysis of the inorganic precursors.

The porous properties of the KLE-templated $CdFe_2O_4$ spinel thin films were also analyzed by nitrogen physisorption measurements at 77 K (see adsorption/desorption isotherms in both Figure 5a and Supporting Information, Figure S4). These data provide a Brunauer–Emmett–Teller (BET) surface area of 220 m^2·cm^{-3} and a pore volume of 1.65×10^{-3} cm^3 for samples heated to 650 °C. The latter value is equivalent to 60% porosity, thereby indicating that the pore cavities in the interior are accessible. We estimate the error margin as being ±10%. However, higher annealing temperatures lead to a slight reduction in both surface area and porosity. Apart from that, it should be noted that samples with a semicrystalline wall structure have a BET surface area of 430 m^2·cm^{-3}, which is approximately twice as large as that of highly crystalline material. This result shows that the restructuring of the pore network between 600 and 650 °C has a profound effect on the porous properties. The pore size distribution was calculated from the adsorption branch using a nonlocal density functional theory (NLDFT) equilibrium model for silica (see Supporting Information, Figure S5). From this analysis, we obtain an average pore size of 12 nm. At first glance, this dimension appears to be underestimated when compared to the pore size determined from electron microscopy. However, pore shape transformation from spherical to oblate during unidirectional lattice contraction has to be taken into account and, in so doing, the value of 12 nm is reasonable.

Because cadmium ferrite has potential for use in magneto-optical devices,[21] the optical properties of the thin films were also examined. Optical absorption measurements (see Figure 5b) conducted on a sample heated to 650 °C indicate direct and indirect band gaps at room temperature of (2.15 ± 0.05) eV and (1.93 ± 0.05) eV, respectively, due to oxygen–metal charge transfer (also referred to as ligand-to-metal charge transfer), that is, excitation from O 2p to Fe 3d (here Fe^{3+} ions on octahedral sites).[43] These values are in fair agreement with literature data for related materials.[44,45] In addition, we find another transition at approximately 2.6 eV, which is assumed to arise from so-called antisite defects, cation disorder, often observed in nanocrystalline ferrites. According to Pailhe et al., this transition is also related to oxygen–metal charge transfer but involves Fe^{3+} ions on tetrahedral sites.[43] They attributed the higher transition energy to the fact that the Fe–O bonds in [FeO_4] tetrahedra are shorter than in [FeO_6] octahedra. We note that a more detailed analysis of the optical properties
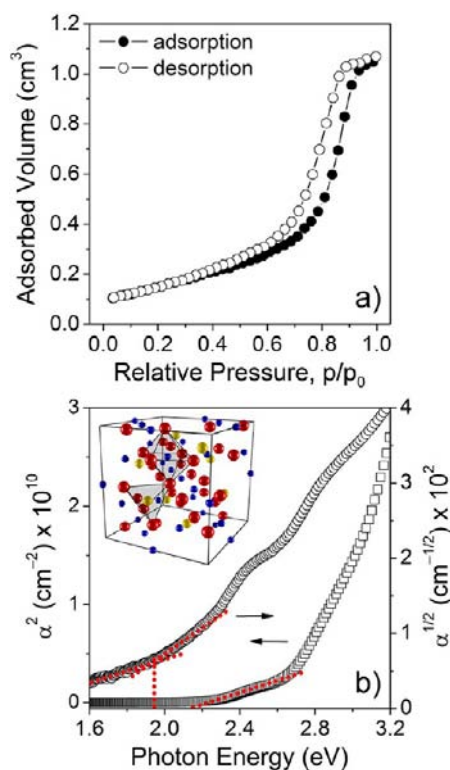
Figure 5. (a) N_2-adsorption/desorption isotherms for approximately 465 nm thick, KLE-templated $CdFe_2O_4$ spinel thin films with a total area of 57 cm^2 heated to 650 °C. The type-IV shape is characteristic of a material with interconnected mesopore cavities. (b) Plots for both direct ($\square$) and indirect ($\bigcirc$) optical transitions. The unit cell for cubic $CdFe_2O_4$ with a normal spinel structure is shown in the inset of panel (b). The unit cell contains 56 atoms, equivalent to eight formula units $CdFe_2O_4$. In this structure, the magnetic Fe^{3+} ions (blue) are located on octahedral 16d sites and the nonmagnetic Cd^{2+} ions (yellow) occupy tetrahedral 8a sites (Wyckoff notation). O^{2-} ions on 32e sites are shown in red.[46] It should be noted that the ionic radii were reduced by a factor of 3 and that two additional O^{2-} ions were added to draw the tetrahedron.

needs a powerful theory to account for all the possible inter- and intra-atomic transitions and, thus, the assignment was made with the help of reports on both $MgFe_2O_4$ and $ZnFe_2O_4$.[43]

As mentioned in the introduction, $CdFe_2O_4$ is a member of the oxide spinel group with the general formula AB_2O_4. The cation distribution in such materials is typically represented by the inversion parameter, λ, with $(A_{1-\lambda}B_\lambda)^{tet}(A_\lambda B_{2-\lambda})^{oct}O_4$. In a normal spinel such as microcrystalline $CdFe_2O_4$ (see inset of Figure 5b), which shows virtually no inversion ($\lambda \approx 0.05$),[47] the single A cation occupies the tetrahedral 8a Wyckoff site while the two B cations are located on two equivalent octahedral 16d sites. In contrast, in an inverse spinel such as microcrystalline $CoFe_2O_4$, one of the B cations is located on the tetrahedral site while both the single A cation and the other B cation occupy the two octahedral coordination sites randomly. But independent of that, the O^{2-} ions form a cubic close-packed structure and occupy the 32e Wyckoff sites. Overall, this means that there are two ordered configurations with $\lambda = 0$ (normal) and $\lambda = 1$ (inverse). However, many spinels, in particular nanocrystalline forms of these materials, exhibit either a partially inverted structure or even a random cation distribution. Taking into account that the KLE-templated $CdFe_2O_4$ thin films studied in this work are solution processed

via sol–gel methods, nanocrystalline, and further also highly textured, they are expected to show an inversion parameter different from that reported for microcrystalline materi-al.[39,48–50]

To obtain information about the crystallization behavior, chemical composition, electronic bonding configuration, and the cation distribution, a series of X-ray diffraction (XRD), Raman spectroscopy, and X-ray photoelectron spectroscopy (XPS) measurements were carried out. Figure 6a shows XRD
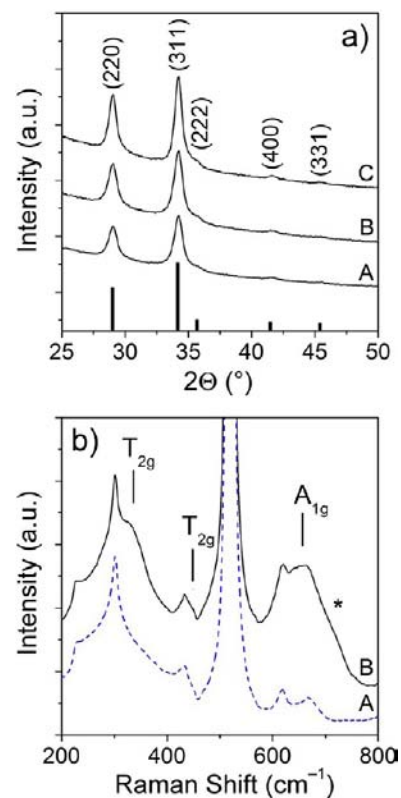

Figure 6. (a) XRD patterns obtained on a KLE-templated $CdFe_2O_4$ spinel thin film heated to different annealing temperatures of 600 °C (A), 650 °C (B), and 700 °C (C). The line pattern shows JCPDS reference card no. 22-1063 for cubic $CdFe_2O_4$ with space group $Fd\bar{3}m$ (O_h^7). (b) Raman spectra for both a reference Si(100) wafer (A) and a KLE-templated thin film on Si(100) heated to 650 °C (B). The asterisk at approximately 727 cm^{-1} indicates an otherwise forbidden Raman mode.

patterns measured in grazing incidence geometry as a function of annealing temperature. The crystallization begins at $\vartheta = (590 \pm 10)$ °C. The average grain size was determined by applying the Scherrer equation to the line broadening of both the (220) and the (311) peaks of cubic $CdFe_2O_4$ at $2\Theta = 29.04°$ and $2\Theta = 34.21°$, respectively. All three diffractograms in panel (a) of Figure 6 were fitted using Gaussian–Lorentzian functions. The Scherrer analysis provides grain sizes of approximately 11 nm at 600 °C, 13 nm at 650 °C, in agreement with the results from HRTEM, and 14 nm at 700 °C. The finding that both the grain size and the wall thickness are virtually of the same order helps explain why the pore structure does not collapse during the course of crystallization. Furthermore, XRD does not indicate the formation of impurity phases such as α-Fe_2O_3 (hematite), which could potentially be formed in the iron-rich material at elevated annealing temperatures.

In the following sections, we specifically focus on KLE-templated $CdFe_2O_4$ thin films heated to 650 °C because of the apparent high degree of crystallinity and the fact that the nanoscale structure is more defined compared to samples heated to 700 °C, as evidenced by electron microscopy and GISAXS. Figure 6b shows a typical Raman spectrum of a sample on a partially oxidized Si(100) wafer (see also Raman spectrum of the bare Si(100) wafer in Supporting Information, Figure S6). According to group theory, defect-free $CdFe_2O_4$ with a normal spinel structure has five first-order Raman-active phonon modes in the frequency range between 200 cm^{-1} and 850 cm^{-1}.[51] However, only three of them can be observed as broad bands at 331 cm^{-1} (T_{2g}), 446 cm^{-1} (T_{2g}), and 652 cm^{-1} (A_{1g}) because of superposition of the spectrum from the substrate. We note that line broadening is a result of finite size effects (phonon confinement). The band assignment is in agreement with data reported previously for both polycrystalline and single-crystalline $ZnFe_2O_4$.[52,53] In addition to these Raman modes, we find a shoulder band at approximately 727 cm^{-1}. The appearance of this band, which is not predicted by group theory, can most likely be associated with antisite defects, that is, some kind of cation distribution among the tetrahedral and octahedral sites. This hypothesis is supported by the finding that single crystals of $MgFe_2O_4$ with $\lambda = 0.78$ show the same features in the high-frequency range between 600 cm^{-1} and 750 cm^{-1}.[54]

Lastly, the cation distribution was quantitatively characterized by XPS because the results with both Raman and UV−vis spectroscopy seem to point to the likelihood of disorder effects. In this context, we note again that microcrystalline $CdFe_2O_4$ shows virtually no inversion with $\lambda \approx 0.05$. Figure 7 depicts
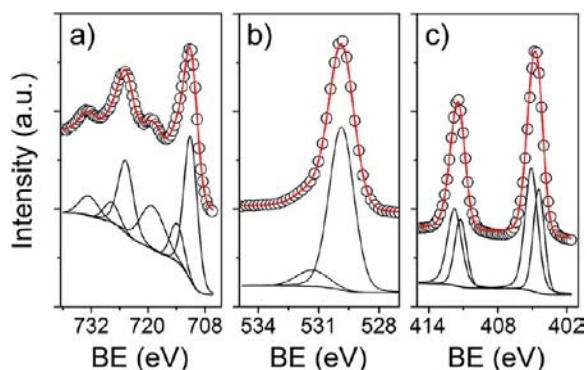

Figure 7. XPS detail spectra of the Fe 2p (a), O 1s (b), and Cd 3d (c) core level regions of KLE-templated $CdFe_2O_4$ spinel thin films heated to 650 °C. Solid lines in black are Gaussian−Lorentzian fits to the experimental data and solid lines in red correspond to the sum of the peak fits. The Shirley method was applied to subtract backgrounds.

XPS detail spectra of the Fe 2p, O 1s, and Cd 3d core level regions. A survey spectrum is given in Supporting Information, Figure S7. Apart from a weak C 1s peak, which we associate with adventitious hydrocarbon, only iron, cadmium, and oxygen core levels can be observed. The Fe 2p spectrum in panel (a) contains a single doublet due to spin−orbit splitting along with strong satellite peaks. The appearance of satellites approximately 8 eV higher in binding energy than the main peaks is characteristic of Fe^{3+}. The apparent asymmetry of the Fe 2p lines already suggests that the inversion parameter must be larger than 0.05. The main peaks at binding energies of (724.72 ± 0.05) eV and (710.99 ± 0.05) eV for the $2p_{1/2}$ and $2p_{3/2}$

lines, respectively, can be assigned to Fe^{3+} ions on octahedral sites and the minor peaks at (727.67 ± 0.05) eV and (713.89 ± 0.05) eV to those on tetrahedral sites.[39,55,56] Table 1

Table 1. XPS Peak Analysis

core level	peak position (eV)[a]	area ratio
Cd $3d_{5/2}$ (oct)	404.52	
Cd $3d_{5/2}$ (tet)	405.00	0.677
Cd $3d_{3/2}$ (oct)	411.27	
Cd $3d_{3/2}$ (tet)	411.75	0.678
Fe $2p_{3/2}$ (oct)	710.99	
Fe $2p_{3/2}$ (tet)	713.89	3.952
Fe $2p_{1/2}$ (oct)	724.72	
Fe $2p_{1/2}$ (tet)	727.67	3.921

[a]Error margin: $\pm$ 0.05 eV.

summarizes the main results from XPS analysis. By comparing the different peak areas, we obtain an inversion parameter $\lambda = 0.40 \pm 0.02$, which corresponds to $(Cd_{0.6}Fe_{0.4})^{tet}(Cd_{0.4}Fe_{1.6})^{oct}O_4$. Deconvolution of the O 1s spectrum in panel (b) indicates two different oxygen bonding states. The main peak at (529.84 ± 0.05) eV can be attributed to oxygen in $CdFe_2O_4$, in line with literature reports, and the shoulder peak at (531.33 ± 0.05) eV can be assigned to hydroxyl groups at the top surface.[57] To verify the accuracy of the determined value of λ, we also examined the Cd 3d spectrum in panel (c) in detail. Both the $3d_{3/2}$ and $3d_{5/2}$ lines can be fit to two peaks. By analogy to the Fe 2p core level, the peaks at binding energies of (411.27 ± 0.05) eV and (404.52 ± 0.05) eV for the $3d_{3/2}$ and $3d_{5/2}$ lines, respectively, can be assigned to Cd^{2+} ions on octahedral sites and those at (411.75 ± 0.05) eV and (405.00 ± 0.05) eV to Cd^{2+} ions on tetrahedral sites. As can be seen, the peak areas of the different $3d_{3/2}$ and $3d_{5/2}$ lines are rather similar and, in fact, we find the same inversion parameter. Overall, the XPS, Raman and UV−vis spectroscopy data lead us to conclude that the mesoporous $CdFe_2O_4$ thin films exhibit a "partially" inverted spinel structure after heating to 650 °C.

The magnetic properties were investigated by SQUID magnetometry for the temperature range of 2−380 K in magnetic fields up to ± 50 kOe. Figure 8a shows typical zero-field-cooled (ZFC)/field-cooled (FC) curves measured both in 100 Oe and in 1000 Oe for different applied field directions, with the plane of the substrate perpendicular ($\perp$) and parallel ($\parallel$) to the external magnetic field. From the data obtained with 100 Oe it can be seen that the direct current (dc) magnetic susceptibility continuously increases with decreasing temperature until a maximum (T_{max}) is reached at approximately 58 K($\parallel$) and 54 K($\perp$), respectively. The fact that the absolute value of the magnetic susceptibility and T_{max} differ among both field directions is most likely related to the morphological anisotropy of the films and the strain anisotropy resulting from unidirectional contraction during thermal treatment (see Figure 3).[37,39] Upon further cooling, the FC curve diverges from the ZFC curve and the FC data decrease slightly until reaching a saturation value at approximately 8 K. The results from ZFC/FC measurements on the same KLE-templated $CdFe_2O_4$ thin film but in 1000 Oe indicate a similar trend in the data. However, it is apparent that the maximum becomes broader and tends to shift to lower temperatures. This behavior resembles the properties of canonical spin glasses.[58−61] In addition, the FC data appear to be virtually independent of temperature below T_{max}. Apart from these features, it is known
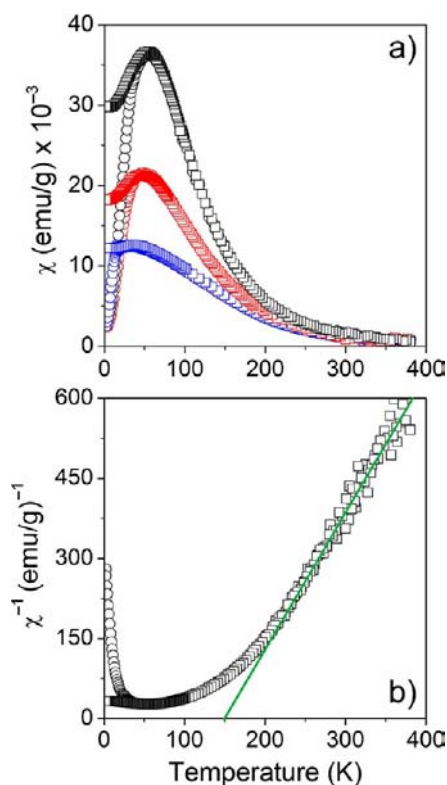
Figure 8. (a) ZFC (O) and FC (□) curves for different applied field directions ($H_{\parallel}$ (black), $H_{\perp}$ (red)) measured at H = 100 Oe. The blue curves represent in-plane ZFC/FC data obtained with 1000 Oe. (b) Inverse in-plane magnetic susceptibility as a function of temperature at $H_{\parallel}$ = 100 Oe. The solid line in green shows the best fit to the Curie–Weiss law.

Figure 9. (a) $M(H)$ plots for different applied field directions ($H_{\parallel}$ (□), $H_{\perp}$ (O)) measured at 5 K (red) and 300 K (black). (b) In- and off-plane hysteresis loops at 5 K in the field range of ±5 kOe. (c) In-plane hysteresis experiment at 300 K. Solid lines show fits to the data using eq 1. Linear susceptibility term, blue; Langevin term, red; sum of fits, green.

that the point (T_{irr}) at which the divergence between the ZFC and FC curves is observed can be used to qualitatively distinguish between spin glass and superparamagnetic materials. The dc magnetic susceptibility data in Figure 8a indicate that T_{irr} equals approximately T_{max}. While in canonical spin glasses the irreversibility typically begins at approximately T_{max} (i.e., $T_{irr} \approx T_{max}$), below which the FC data are largely independent of temperature, in superparamagnets the FC curve diverges from the ZFC curve at temperatures above T_{max} (i.e., $T_{irr} > T_{max}$) and the FC data continue to rise as the temperature is decreased further. Overall, these results point to a low-temperature spin glass-like state.

As shown in Figure 8b, the high-temperature dc magnetic susceptibility follows a Curie–Weiss behavior ($\chi = C/(T - \theta_{CW})$) with a positive Weiss temperature θ_{CW} = 147 K and Curie constant C = 0.4 emu·K·g^{-1}. We note that the latter value is more than 10 times larger than that expected for paramagnetic CdFe$_2$O$_4$. Both the discrepancy between measured susceptibility and paramagnetic behavior and the nonlinear isothermal magnetization at 300 K (see Figure 9) are indicative of at least partial superparamagnetism.

Figure 9 shows magnetization versus field ($M(H)$) data for both applied field directions measured at 5 and 300 K. From panel (a) it is apparent that the magnetization is not completely saturated at 5 K, which is in agreement with the presence of a glassy magnetic state. Similar observations have been made for various nanomaterials and have often been associated with spin canting, spin freezing, and so forth.[34,62−64] Even though the origin of these effects is not fully understood yet, it is typically
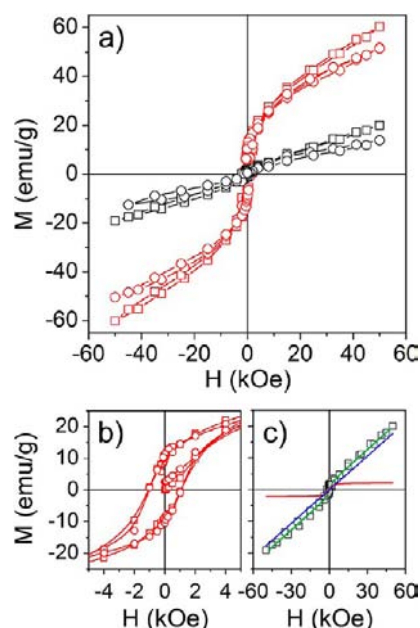
attributed to magnetic frustration, (surface) disorder/anisotropy, and finite size effects. From the same data it can be seen that in-plane hysteresis experiments yield slightly higher magnetization values, which indicates that the easy axis for magnetic alignment lies parallel to the plane of the substrate. This is not surprising, however, given the morphological anisotropy of the films and the resulting magnetic anisotropy. The in- and off-plane hysteresis loops in panel (b) show that the mesoporous material in fact exhibits ferrimagnetic behavior at 5 K: the positive Weiss temperature is characteristic of ferrimagnetic spin coupling below 147 K. The coercive field (H_c) is determined to be approximately 1 kOe and appears to be independent of film orientation.

As mentioned above, KLE-templated CdFe$_2$O$_4$ thin films exhibit nonlinear magnetization at 300 K: the remanent magnetization (M_r) is comparatively small but not zero as for purely paramagnetic materials. Such profiles can be understood as arising from the presence of superparamagnetic clusters in an otherwise paramagnetic environment. Panel (c) of Figure 9 shows a typical in-plane hysteresis curve measured at 300 K. These data can be successfully fitted using a simple Langevin model ($L(x)$) and an additional paramagnetic linear susceptibility term ($k·H$) according to:

$$M = M_0 \cdot L(x) + k \cdot H \tag{1}$$

where $L(x) = \coth(x) - 1/x$ and $x = \mu \cdot H/(k_B \cdot T)$. In these equations, M_0 is the magnetization of the superparamagnetic part of the sample, k is the susceptibility, μ is the magnetic moment per cluster, k_B is the Boltzmann constant, and T represents the temperature. From the fits to the data, we obtain M_0 = 2.1 emu·g^{-1}, k = 3.5 × 10^{-4} emu·(Oe·g)$^{-1}$, and μ = 4800 μ_B. Using both the magnetic moment of the clusters and the saturation magnetization (M_S) at 5 K and assuming further that they have a spherical shape, the average cluster size is calculated

to be 7 nm in diameter. Although this value seems reasonable at first glance, we note that it is only a rough estimate.

Alternating current (ac) magnetic susceptibility experiments were also carried out to better characterize the low-temperature magnetic state of the KLE-templated $CdFe_2O_4$ thin films and to find out whether T_{max} (see dc magnetic susceptibility data in Figure 8a) represents a freezing temperature (T_f, for spin glasses) or a blocking temperature (T_b, for superparamagnets). Figure 10 shows the real part (in-phase component) of the ac
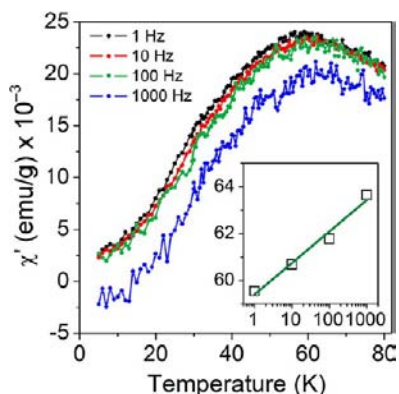

Figure 10. Temperature dependence of the real part of the ac magnetic susceptibility for different frequencies at H_{ac} = 6.5 Oe. Both the frequency dependence of the peak temperature (T_p (K) versus ν (Hz)) and a linear fit (green line) to the data are shown in the inset.

magnetic susceptibility versus temperature ($\chi'(T)$) for different driving frequencies (ν) of 1 Hz, 10 Hz, 100 Hz, and 1000 Hz. The amplitude of the ac field (H_{ac}) was kept constant at 6.5 Oe during the experiments. As expected, $\chi'(T)$ is frequency-dependent: the peak temperature (T_p), which is at low frequency similar to T_{max}, shifts to higher values with increasing frequency. In recent years, it has been shown that the frequency dependence of the peak temperature can be used to distinguish between superparamagnetic blocking and spin glass freezing. To do so, we calculated the frequency sensitivity (p), which is defined as $p = \Delta T_p/(T_p\cdot\Delta\log(\omega))$ with $\omega = 2\pi\cdot\nu$. The green line in the inset of Figure 10 is the best fit to the data and yields a frequency sensitivity of 0.021. This value is in the range typically observed for canonical spin glasses;[65] the frequency sensitivity of the peak temperature expected for superparamagnetic blocking is usually 1 order of magnitude greater.[66] Overall, all magnetic susceptibility data seem to point to the likelihood of spin glass behavior below a characteristic temperature $T_f \approx 60$ K. This conclusion is further supported by the fact that the Arrhenius-type dependence of the peak temperature variation with driving frequency yields unphysical parameter values, which have also been found for other spin glass compounds (see Supporting Information, Figure S8).[67,68]

Lastly, we note that the magnetic properties of the material employed here differ significantly from those of single crystals. Such single crystals reveal an anomaly in susceptibility at 13 K and have a negative Weiss temperature of −53 K, as described by Kamazawa et al.[69] They associated these features with an ordering transition temperature and strong geometrical frustration, respectively. We assume that the discrepancy between the results of our analyses and the results reported by Kamazawa et al. is due to a combination of effects such as cation disorder, magnetic frustration, interactions among the

superparamagnetic clusters, finite-size effects, and so forth. In this regard, it is important to note that particle interactions (dipolar, direct exchange, etc.) have been shown to have a profound effect on the overall magnetic behavior of nanomaterials and can lead to so-called supermagnetism (super spin glass or super ferromagnetism).[70] As can be clearly seen from HRTEM imaging in Figure 2, adjacent single-domain spinel grains in the pore walls of the KLE-templated $CdFe_2O_4$ thin films touch each other and, thus, interactions among them are very likely to come into play.

■ CONCLUSION

The present work shows that ordered large-pore mesoporous $CdFe_2O_4$ thin films can be readily synthesized through polymer templating of hydrated nitrate salt precursors. The morphology, microstructure, and magnetic properties of samples heated to 650 °C in air were characterized in detail by a combination of SEM, AFM, HRTEM, STEM-HAADF, GISAXS, XRD, XPS, UV−vis and Raman spectroscopy. The results obtained demonstrate that the pore structure can be mostly preserved during conversion of the amorphous material to single-phase spinel and that the walls consist of spherical grains averaging 13 nm in diameter. Furthermore, they show that the cation distribution among the tetrahedral and octahedral sites differs significantly from that observed for microcrystalline $CdFe_2O_4$. Both ac and dc magnetic susceptibility measurements further confirm the quality of the mesoporous thin films with a positive Weiss temperature (θ_{CW} = 147 K) and low-temperature spin glass-like behavior. In addition, closer examination of the room temperature magnetization data indicates the presence of sub-10 nm diameter superparamagnetic clusters in an otherwise paramagnetic matrix.

Overall, the data shown in this work lead us to conclude that the KLE-templated $CdFe_2O_4$ spinel thin films are well-defined at both the nanoscale and the microscale. It should be noted that nanocrystalline materials with an ordered mesoporous morphology similar to those here could pave the way for the development of nanoenabled device design. For example, 3-dimensional networks of interconnected pores might facilitate the formation of novel nanocomposites with intimate contact and multifunctional properties. Future work will be dedicated to producing two-phase (e.g., magnetically exchange-coupled) materials by filling the pores using such methods as incipient wetness impregnation and sputtering.

■ ASSOCIATED CONTENT

Ⓢ Supporting Information
Low-magnification top view SEM, STEM-HAADF, and HRTEM images at different magnifications. SAXS patterns. N_2-adsorption/desorption isotherms and pore size distribution. XPS survey spectrum. Arrhenius-type plot of the peak temperature variation with driving frequency. Reference Raman spectrum of Si(100). This material is available free of charge via the Internet at http://pubs.acs.org.

■ AUTHOR INFORMATION

Corresponding Author
*E-mail: torsten.brezesinski@kit.edu. Phone: +49 721 608-28827.

Present Address
⊥Helmholtz Institute Ulm (HIU) Electrochemical Energy Storage, Albert-Einstein-Allee 11, 89081 Ulm, Germany.

■ **REFERENCES**

(1) Zukalova, M.; Zukal, A.; Kavan, L.; Nazeeruddin, M. K.; Liska, P.; Gratzel, M. *Nano Lett.* **2005**, *5*, 1789−1792.

(2) Hartmann, P.; Lee, D. K.; Smarsly, B. M.; Janek, J. *ACS Nano* **2010**, *4*, 3147−3154.

(3) Brezesinski, K.; Haetge, J.; Wang, J.; Mascotto, S.; Reitz, C.; Rein, A.; Tolbert, S. H.; Perlich, J.; Dunn, B.; Brezesinski, T. *Small* **2011**, *7*, 407−414.

(4) Vu, A.; Qian, Y.; Stein, A. *Adv. Energy Mater.* **2012**, *2*, 1056−1085.

(5) Ren, Y.; Ma, Z.; Bruce, P. G. *Chem. Soc. Rev.* **2012**, *41*, 4909−4927.

(6) Yang, P. D.; Zhao, D. Y.; Margolese, D. I.; Chmelka, B. F.; Stucky, G. D. *Nature* **1998**, *396*, 152−155.

(7) Choi, S. Y.; Mamak, M.; Coombs, N.; Chopra, N.; Ozin, G. A. *Adv. Funct. Mater.* **2004**, *14*, 335−344.

(8) Grosso, D.; Boissiere, C.; Smarsly, B.; Brezesinski, T.; Pinna, N.; Albouy, P. A.; Amenitsch, H.; Antonietti, M.; Sanchez, C. *Nat. Mater.* **2004**, *3*, 787−792.

(9) Szeifert, J. M.; Feckl, J. M.; Fattakhova-Rohlfing, D.; Liu, Y.; Kalousek, V.; Rathousky, J.; Bein, T. *J. Am. Chem. Soc.* **2010**, *132*, 12605−12611.

(10) Sanchez, C.; Boissiere, C.; Grosso, D.; Laberty, C.; Nicole, L. *Chem. Mater.* **2008**, *20*, 682−737.

(11) Kresge, C. T.; Leonowicz, M. E.; Roth, W. J.; Vartuli, J. C.; Beck, J. S. *Nature* **1992**, *359*, 710−712.

(12) Lu, Y. F.; Ganguli, R.; Drewien, C. A.; Anderson, M. T.; Brinker, C. J.; Gong, W. L.; Guo, Y. X.; Soyez, H.; Dunn, B.; Huang, M. H.; Zink, J. I. *Nature* **1997**, *389*, 364−368.

(13) Brinker, C. J.; Lu, Y. F.; Sellinger, A.; Fan, H. Y. *Adv. Mater.* **1999**, *11*, 579−585.

(14) Corma, A.; Atienzar, P.; Garcia, H.; Chane-Ching, J. Y. *Nat. Mater.* **2004**, *3*, 394−397.

(15) Deshpande, A. S.; Pinna, N.; Smarsly, B.; Antonietti, M.; Niederberger, M. *Small* **2005**, *1*, 313−316.

(16) Rauda, I. E.; Buonsanti, R.; Saldarriaga-Lopez, L. C.; Benjauthrit, K.; Schelhas, L. T.; Stefik, M.; Augustyn, V.; Ko, J.; Dunn, B.; Wiesner, U.; Milliron, D. J.; Tolbert, S. H. *ACS Nano* **2012**, *6*, 6386−6399.

(17) Buonsanti, R.; Pick, T. E.; Krins, N.; Richardson, T. J.; Helms, B. A.; Milliron, D. J. *Nano Lett.* **2012**, *12*, 3872−3877.

(18) Brezesinski, T.; Antonietti, M.; Smarsly, B. M. *Adv. Mater.* **2007**, *19*, 1074−1078.

(19) Chen, N. S.; Yang, X. J.; Liu, E. S.; Huang, J. L. *Sens. Actuators, B* **2000**, *66*, 178−180.

(20) Lou, X.; Liu, S.; Shi, D.; Chu, W. *Mater. Chem. Phys.* **2007**, *105*, 67−70.

(21) Bakuzis, A. F.; Neto, K. S.; Gravina, P. P.; Figueiredo, L. C.; Morais, P. C.; Silva, L. P.; Azevedo, R. B.; Silva, O. *Appl. Phys. Lett.* **2004**, *84*, 2355−2357.

(22) Sugimoto, M. *J. Am. Ceram. Soc.* **1999**, *82*, 269−280.

(23) Nan, C. W.; Bichurin, M. I.; Dong, S. X.; Viehland, D.; Srinivasan, G. *J. Appl. Phys.* **2008**, *103*, 031101.

(24) Willard, M. A.; Kurihara, L. K.; Carpenter, E. E.; Calvin, S.; Harris, V. G. *Int. Mater. Rev.* **2004**, *49*, 125−170.

(25) Bera, S.; Prince, A. A. M.; Velmurugan, S.; Raghavan, P. S.; Gopalan, R.; Panneerselvam, G.; Narasimhan, S. V. *J. Mater. Sci.* **2001**, *36*, 5379−5384.

(26) Wu, J.; Li, N.; Xu, J.; Jiang, Y.; Ye, Z. G.; Xie, Z.; Zheng, L. *Appl. Phys. Lett.* **2011**, *99*, 202505.

(27) Chen, J. P.; Sorensen, C. M.; Klabunde, K. J.; Hadjipanayis, G. C.; Devlin, E.; Kostikas, A. *Phys. Rev. B* **1996**, *54*, 9288−9296.

(28) Chinnasamy, C. N.; Narayanasamy, A.; Ponpandian, N.; Joseyphus, R. J.; Jeyadevan, B.; Tohji, K.; Chattopadhyay, K. *J. Magn. Magn. Mater.* **2002**, *238*, 281−287.

(29) Rajendran, M.; Pullar, R. C.; Bhattacharya, A. K.; Das, D.; Chintalapudi, S. N.; Majumdar, C. K. *J. Magn. Magn. Mater.* **2001**, *232*, 71−83.

(30) Li, D.; Herricks, T.; Xia, Y. *Appl. Phys. Lett.* **2003**, *83*, 4586.

(31) Nlebedim, I. C.; Snyder, J. E.; Moses, A. J.; Jiles, D. C. *J. Magn. Magn. Mater.* **2010**, *322*, 3938−3942.

(32) Chinnasamy, C. N.; Narayanasamy, A.; Ponpandian, N.; Joseyphus, R. J.; Chattopadhyay, K.; Shinoda, K.; Jeyadevan, B.; Tohji, K.; Nakatsuka, K.; Greneche, J.-M. *J. Appl. Phys.* **2001**, *90*, 527.

(33) Chen, Q.; John Zhang, Z. *Appl. Phys. Lett.* **1998**, *73*, 3156.

(34) Dormann, J. L.; Nogues, M. *J. Phys.: Condens. Matter* **1990**, *2*, 1223−1237.

(35) Schlaad, H.; Kukula, H.; Rudloff, J.; Below, I. *Macromolecules* **2001**, *34*, 4302−4304.

(36) Thomas, A.; Schlaad, H.; Smarsly, B.; Antonietti, M. *Langmuir* **2003**, *19*, 4455−4459.

(37) Quickel, T. E.; Le, V. H.; Brezesinski, T.; Tolbert, S. H. *Nano Lett.* **2010**, *10*, 2982−2988.

(38) Haetge, J.; Suchomski, C.; Brezesinski, T. *Inorg. Chem.* **2010**, *49*, 11619−11626.

(39) Reitz, C.; Suchomski, C.; Haetge, J.; Leichtweiss, T.; Jaglicic, Z.; Djerdj, I.; Brezesinski, T. *Chem. Commun.* **2012**, *48*, 4471−4473.

(40) Wojciechowski, K. T.; Malecki, A. *Thermochim. Acta* **1999**, *331*, 73−77.

(41) Wieczorek-Ciurowa, K.; Kozak, A. J. *J. Therm. Anal. Calorim.* **1999**, *58*, 647−651.

(42) Malecki, A.; Gajerski, R.; Labus, S.; Prochowska-Klisch, B.; Wojciechowski, K. T. *J. Therm. Anal. Calorim.* **2000**, *60*, 17−23.

(43) Pailhe, N.; Wattiaux, A.; Gaudon, M.; Demourgues, A. *J. Solid State Chem.* **2008**, *181*, 1040−1047.

(44) Miao, F.; Deng, Z.; Lv, X.; Gu, G.; Wan, S.; Fang, X.; Zhang, Q.; Yin, S. *Solid State Commun.* **2010**, *150*, 2036−2039.

(45) Gao, D.; Shi, Z.; Xu, Y.; Zhang, J.; Yang, G.; Zhang, J.; Wang, X.; Xue, D. *Nanoscale Res. Lett.* **2010**, *5*, 1289−1294.

(46) Sickafus, K. E.; Wills, J. M.; Grimes, N. W. *J. Am. Ceram. Soc.* **1999**, *82*, 3279−3292.

(47) Krezhov, K.; Konstantinov, P.; Asenov, S. *Phys. B* **2000**, *276*, 636−637.

(48) Mahmoud, M. H.; Abdallas, A. M.; Hamdeh, H. H.; Hikal, W. M.; Taher, S. M.; Ho, J. C. *J. Magn. Magn. Mater.* **2003**, *263*, 269−274.

(49) Sepelak, V.; Indris, S.; Heitjans, P.; Becker, K. D. *J. Alloys Compd.* **2007**, *434*, 776−778.

(50) Desai, R.; Mehta, R. V.; Upadhyay, R. V.; Gupta, A.; Praneet, A.; Rao, K. V. B. *Mater. Sci.* **2007**, *30*, 197−203.

(51) White, W. B.; Deangelis, B. A. *Spectrochim. Acta A-M.* **1967**, *A 23*, 985−995.

(52) Singh, J. P.; Srivastava, R. C.; Agrawal, H. M.; Kumar, R. *J. Raman Spectrosc.* **2011**, *42*, 1510−1517.

(53) Wang, Z.; Schiferl, D.; Zhao, Y.; O'Neill, H. S. C. *J. Phys. Chem. Solids* **2003**, *64*, 2517−2523.

(54) Wang, Z.; Lazor, P.; Saxena, S. K.; O'Neill, H. S. C. *Mater. Res. Bull.* **2002**, *37*, 1589−1602.

(55) Zhou, Z.; Zhang, Y.; Wang, Z.; Wei, W.; Tang, W.; Shi, J.; Xiong, R. *Appl. Surf. Sci.* **2008**, *254*, 6972−6975.

(56) Gu, Z. J.; Xiang, X.; Fan, G. L.; Li, F. *J. Phys. Chem. C* **2008**, *112*, 18459−18466.

3753

dx.doi.org/10.1021/ic302283q | *Inorg. Chem.* 2013, 52, 3744−3754

(57) Liu, Y.; Jiang, W.; Xu, L.; Yang, X.; Li, F. *Mater. Lett.* **2009**, *63*, 2526−2528.

(58) Mydosh, J. A. *Spin Glasses: An Experimental Introduction*; Taylor & Francis: London, U.K., 1993.

(59) Chatterjee, S.; Nigam, A. K. *J. Phys. Rev. B* **2002**, *66*, 104403.

(60) Goya, G. F.; Memo, A.; Haeuseler, H. *J. Solid State Chem.* **2002**, *164*, 326−331.

(61) Dolia, S. N.; Prasad, A. S.; Dhawan, M. S.; Sharma, M. P.; Chander, S. *Hyperfine Interact.* **2008**, *184*, 75−81.

(62) Kodama, R. H.; Berkowitz, A. E.; McNiff, E. J.; Foner, S. *Phys. Rev. Lett.* **1996**, *77*, 394−397.

(63) Jiang, J. Z.; Goya, G. F.; Rechenberg, H. R. *J. Phys.: Condens. Matter* **1999**, *11*, 4063−4078.

(64) Chinnasamy, C. N.; Narayanasamy, A.; Ponpandian, N.; Chattopadhyay, K.; Shinoda, K.; Jeyadevan, B.; Tohji, K.; Nakatsuka, K.; Furubayashi, T.; Nakatani, I. *Phys. Rev. B* **2001**, *63*, 184108.

(65) De Toro, J. A.; Lopez de la Torre, M. A.; Riveiro, J. M.; Bland, J.; Goff, J. P.; Thomas, M. F. *J. Appl. Phys.* **2002**, *91*, 8396.

(66) Tackett, R. J.; Parsons, J. G.; Machado, B. I.; Gaytan, S. M.; Murr, L. E.; Botez, C. E. *Nanotechnology* **2010**, *21*, 365703.

(67) Goldfarb, R. B.; Patton, C. E. *Phys. Rev. B* **1981**, *24*, 1360−1373.

(68) Nadeem, K.; Krenn, H.; Traussnig, T.; Wurschum, R.; Szabo, D. V.; Letofsky-Papst, I. *J. Appl. Phys.* **2012**, *111*, 113911.

(69) Kamazawa, K.; Park, S.; Lee, S. H.; Sato, T. J.; Tsunoda, Y. *Phys. Rev. B* **2004**, *70*, 024418.

(70) Knobel, M.; Nunes, W. C.; Socolovsky, L. M.; De Biasi, E.; Vargas, J. M.; Denardin, J. C. *J. Nanosci. Nanotechnol.* **2008**, *8*, 2836−2857.